

## Article

# Evaporated MAPbI<sub>3</sub> Perovskite Planar Solar Cells with Different Annealing Temperature

Yi-Tsung Chang <sup>1</sup>, Ching-Ho Tien <sup>2</sup> , Kun-Yi Lee <sup>3</sup>, Yu-Shen Tung <sup>2</sup> and Lung-Chien Chen <sup>2,\*</sup> 

<sup>1</sup> Department of Physics, School of Science, Jimei University, Xiamen 361021, China; oliver\_ytchang@jmu.edu.cn

<sup>2</sup> Department of Electro-Optical Engineering, National Taipei University of Technology, Taipei 10608, Taiwan; chtien@mail.ntut.edu.tw (C.-H.T.); s0323124@gm.ncue.edu.tw (Y.-S.T.)

<sup>3</sup> Department of Electrical Engineering, China University of Science and Technology, Taipei 11581, Taiwan; kelvin119@gmail.com

\* Correspondence: ocean@ntut.edu.tw; Tel.: +886-2-27712171

**Abstract:** The power conversion efficiency (PCE) of an Ag/spiro-OMeTAD/CH<sub>3</sub>NH<sub>3</sub>PbI<sub>3</sub> (MAPbI<sub>3</sub>)/PCBM/mesoporous TiO<sub>2</sub>/compact TiO<sub>2</sub>/FTO planar solar cell with different annealing temperatures of PbI<sub>2</sub> and MAPbI<sub>3</sub> films was investigated in this study. The morphology control of a MAPbI<sub>3</sub> thin film plays key roles in high-efficiency perovskite solar cells. The PbI<sub>2</sub> films were prepared by using thermal vacuum evaporation technology, and the MAPbI<sub>3</sub> perovskite films were synthesized with two-step synthesis. The X-ray spectra and surface morphologies of the PbI<sub>2</sub> and MAPbI<sub>3</sub> films were examined at annealing temperatures of 80, 100, 120, and 140 °C for 10 min. The performance of the perovskite planar solar cell at an annealing temperature of 100 °C for 10 min was demonstrated. The power conversion efficiency (PCE) was about 8.66%, the open-circuit voltage (V<sub>oc</sub>) was 0.965 V, the short-circuit current (J<sub>sc</sub>) was 13.6 mA/cm<sup>2</sup>, and the fill factor (FF) was 0.66 by scanning the density–voltage (J–V) curve.

**Keywords:** perovskite; solar cell; evaporation; MAPbI<sub>3</sub>



**Citation:** Chang, Y.-T.; Tien, C.-H.; Lee, K.-Y.; Tung, Y.-S.; Chen, L.-C. Evaporated MAPbI<sub>3</sub> Perovskite Planar Solar Cells with Different Annealing Temperature. *Energies* **2021**, *14*, 2145. <https://doi.org/10.3390/en14082145>

Academic Editor: Claudia Barolo

Received: 2 March 2021

Accepted: 7 April 2021

Published: 12 April 2021

**Publisher's Note:** MDPI stays neutral with regard to jurisdictional claims in published maps and institutional affiliations.



**Copyright:** © 2021 by the authors. Licensee MDPI, Basel, Switzerland. This article is an open access article distributed under the terms and conditions of the Creative Commons Attribution (CC BY) license (<https://creativecommons.org/licenses/by/4.0/>).

## 1. Introduction

Organic–inorganic halide perovskite solar cells (PSCs) have been presented with a certified power conversion efficiency (PCE) of 25.5% by the National Renewable Energy Laboratory (NREL) [1], and they have become a device material of extensive study owing to their low cost and attractive optoelectronic properties, including the semitransparent properties of perovskite materials [2–4], good flexibility [5–8], large area [9–11], hole transport layer (HTL) [12], electron transport layer (ETL) [13], and so forth, which are comparable to the silicon solar cell [14–18]. However, they are not suitable as commercial solar cells because of the instability of perovskite (CH<sub>3</sub>NH<sub>3</sub>PbI<sub>3</sub> (MAPbI<sub>3</sub>)) solar cells.

Recently, a method for improving perovskite solar cells in terms of power conversion efficiency because of the impacts of defects considers the absorption layer and adjacent interfaces on perovskite [19], the compositional elements of the perovskite [20], the suppression of nonradiative recombination at the perovskite surface and grain boundaries (GBs) [21], and HTL [22,23]. One major challenge of the perovskite solar cell was to pattern periodic nanostructures on large-area thin-film solar cells. Electron beam lithography was used to fabricate nanostructures with well-controlled size, shape, and spacing, but it was impractical with its low sample throughput and high cost. Vacuum and solution processes were the first two main techniques used to prepare perovskite films. Although PSCs prepared by the solution method have made great achievements, the current process of preparing perovskite films through the solution method requires the use of a large amount of organic solvents, such as chlorobenzene (CB), dimethylformamide (DMF), and dimethyl sulfoxide (DMSO). The post-treatment of these organic solvents will be a major

problem that must be faced in the industrialization process. In the dual-source vapor co-deposition process,  $PbX_2$  and  $CH_3NH_3I$  were used as gas sources to obtain dense and high-quality films [24–26]. However, the experimental conditions of this method were harsh and required high-energy-consumption vacuum conditions, and the experimental operation process was relatively uncontrollable. Compared with the solution method, the vacuum vapor deposition technology does not require the use of organic solvents. Its advantages include high surface coverage, low surface roughness, good compatibility with large-area equipment, and precise control of film thickness.

In this paper, a universal and straightforward approach to examine the interface physics of perovskite thin-film solar cells is proposed, and uses a method of two-step spin coating to fabricate perovskite films.  $PbI_2$  films were deposited on an FTO glass substrate by thermal evaporation, and they were annealed at temperatures of 80, 100, 120, and 140 °C for 10 min. Then a methylammonium iodide (MAI) solution containing 50 mg MAI and 1 mL isopropanol (IPA) was dropped onto the  $PbI_2$ /FTO glass substrate in the vacuum [27,28]. The spectra of absorbance, transmittance, SEM, and XRD of  $PbI_2$  and perovskite films on the flat FTO glass substrates were investigated at annealing temperatures of 80, 100, 120, and 140 °C for 10 min, respectively. The 2,2',7,7'-tetrakis(*N,N'*-di-*p*-methoxyphenylamine)-9,9'-spirobifluorene (spiro-OMeTAD) was as the HTL, and the 6,6-phenyl-C61-butyric acid methyl ester (PCBM) was as the ETL, and a solar cell with an Ag/spiro-OMeTAD/MAPbI<sub>3</sub>/PCBM/mesoporous TiO<sub>2</sub>/compact TiO<sub>2</sub>/FTO glass structure performance was fabricated and reported, which demonstrated that the efficiency improvement for the cell with different MAPbI<sub>3</sub> GBs films was induced by light trapping.

## 2. Materials and Methods

Because of the above research background, this paper proposed a solar cell with an organic perovskite (MAPbI<sub>3</sub>) active layer by using of spin-coating and thermal vacuum evaporation technology. The cell structure and energy band diagram for fabricating MAPbI<sub>3</sub> PSC can be found in Figure 1, where the inset shows a schematic illustration of the perovskite MAPbI<sub>3</sub> preparation two-step process. First, the FTO glass substrate was cleaned by an ultrasonic shaker and ultraviolet (UV)–ozone light for 15 min, respectively. Then a PSC was fabricated by lithography technology. The PSC structure size was 5 × 2 mm. PSCs were fabricated with the typical configuration of an Ag/HTM/MAPbI<sub>3</sub>/ETL/FTO structure. The mesoporous TiO<sub>2</sub> film plays the role of scaffold to support perovskite and the electron collector, and its thickness, porosity, and particle size would greatly influence the device's performance. The experiment procedure and measurement are described in detailed as follows.

### 2.1. Fabrication of Mesoporous TiO<sub>2</sub>/Compact TiO<sub>2</sub>/FTO Structure (TiO<sub>2</sub>/FTO)

First, the FTO glass substrate was placed in a beaker containing acetone, alcohol, and IPA solutions, by using ultrasonic and UV–ozone light for 15 min, respectively. The etched-FTO glass substrate size was 1.5 × 1.5 cm. The FTO electrode was patterned by lithography technology, and it was covered with high-temperature-resistant tape. To prepare a compact TiO<sub>2</sub> thin film, the precursor solution was composed of a prediluted titanium diisopropoxide bis(acetylacetonate) solution in absolute ethanol (1:9 weight ratio). The precursor solution of 40 μL TiO<sub>2</sub> was spin-coated onto the patterned-FTO substrate at 3000 rpm for 30 s. The compact TiO<sub>2</sub> thin film of 50 nm thickness was fabricated and annealed at 500 °C in the atmosphere for 30 min.

A milk-tea-colored porous TiO<sub>2</sub> solution with a weight ratio of 1:4 was mixed into a solvent of titanium dioxide nanoparticle slurry (Ti–nanoxide T/SP) and absolute ethanol at room temperature for 12 h as mesoporous TiO<sub>2</sub> precursor. Then 40 μL of porous TiO<sub>2</sub> solution was spin-coated onto the compact TiO<sub>2</sub>/FTO structure at 3000 rpm for 30 s. Then the obtained 200 nm mesoporous TiO<sub>2</sub> layer was annealed at 500 °C for 30 min in ambient air after the heat-resistant tape was removed.

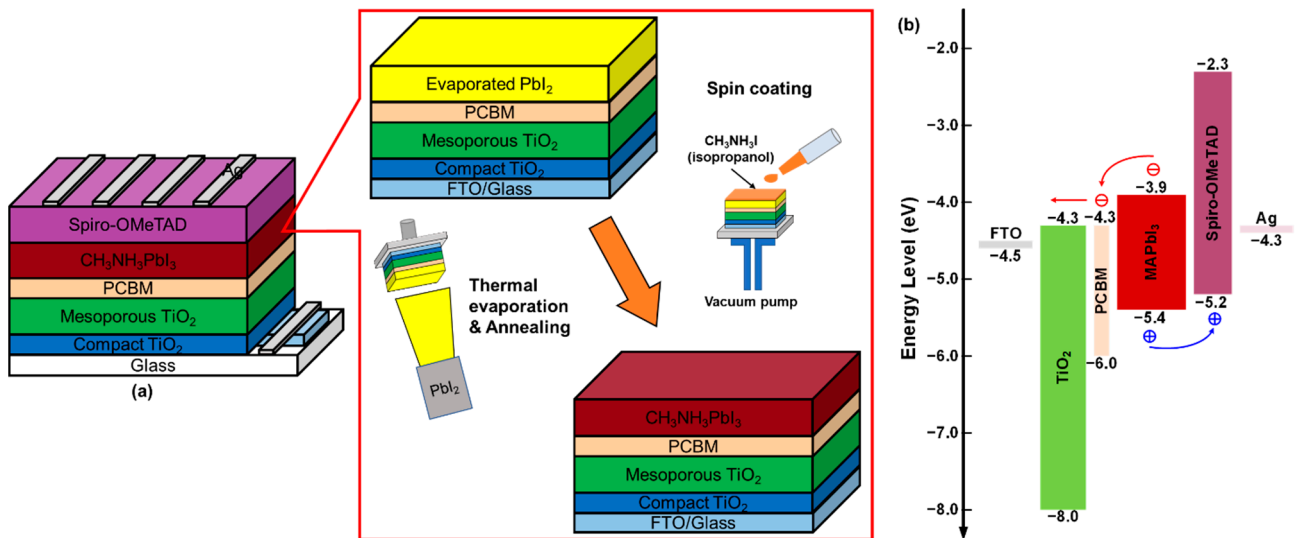


**Figure 1.** Schematic of the (a) perovskite solar cell configuration and (b) energy band diagram. The inset shows a schematic representation of the synthesis of the  $\text{MAPbI}_3$  perovskite film used to create evaporated  $\text{PbI}_2$  in the perovskite film.

### 2.2. Fabrication of PCBM/ $\text{TiO}_2$ /FTO (ETL)

A 2 wt% PCBM solution was obtained at an ambient temperature of 25 °C as the ETL precursor where 20 mg of PCBM was mixed in a solvent of 1 mL of chlorobenzene (CB) by using a magnet stirrer to stir for more than 2 h in a nitrogen glove box. A 50  $\mu\text{L}$  precursor solution was spin-coated onto the mesoporous  $\text{TiO}_2$ /compact  $\text{TiO}_2$ /FTO structure at 2000 rpm for 40 s, and a PCBM film was stored in a nitrogen glove box for 40 min at room temperature.

### 2.3. Fabrication of $\text{MAPbI}_3$ /PCBM/ $\text{TiO}_2$ /FTO (Perovskite)

After the PCBM ETL was formed, a metal mask was covered on the PCBM/ $\text{TiO}_2$ /FTO structure. Then a 130 nm thick  $\text{PbI}_2$  film was thermally evaporated at  $5 \times 10^{-6}$  Torr, and the evaporated rate was about 1.2–1.8 nm/s. Four samples were taken out after the chamber was cooled for 10 min and annealed at temperatures of 80, 100, 120, and 140 °C for 15 min, respectively. An amount of 50 mg of methylammonium iodide (MAI) and 1 mL of IPA solvent were mixed as the perovskite precursor by stirring with a magnetic stirrer. An amount of 40  $\mu\text{L}$  of MAI precursor solution was spin-coated onto a  $\text{PbI}_2$ /PCBM/ $\text{TiO}_2$ /FTO structure. During this process, first, it was dripped in the beginning at 0 rpm for 10 s for it to coat the sample evenly. In the second stage, the precursor solution of perovskite was spin-coated at 2000 rpm for 40 s. Then, the sample was annealed at 100 °C and baked for 10 min. The entire perovskite film was prepared in a nitrogen glove box. The nitrogen glove box needed to be controlled at oxygen and moisture below 0.1 ppm owing to material that was afraid of water and oxygen. This two-step method of forming a film was conducive to the formation of a better texture of a 250 nm thick  $\text{MAPbI}_3$  film.

### 2.4. Fabrication of Spiro-OMeTAD/ $\text{MAPbI}_3$ /PCBM/ $\text{TiO}_2$ /FTO (HTL)

Amounts of 40 mg of spiro-OMeTAD powder, 0.5 mL of chlorobenzene, 14.5  $\mu\text{L}$  of 4-*tert*-butylpyridine (tBP), and 7.5  $\mu\text{L}$  of lithium bis(trifluoromethanesulfonyl)imide (Li-TFSI) were mixed as the spiro-OMeTAD HTL precursor. The Li-TFSI could improve the hole mobility, and its solution consists of dissolving 50 mg of Li-TFSI powder in 0.1 mL of acetonitrile (ACN) solvent. The precursor solution was spin-coated onto a  $\text{MAPbI}_3$ /PCBM/ $\text{TiO}_2$ /FTO structure at 3000 rpm for 30 s. The thickness of p-type HTL was 200 nm. The entire spiro-OMeTAD film was prepared in a nitrogen glove box.

### 2.5. Fabrication of Ag/Spiro-OMeTAD/MAPbI<sub>3</sub>/PCBM/TiO<sub>2</sub>/FTO (PSC)

After an Ag electrode was patterned on the spiro-OMeTAD/MAPbI<sub>3</sub>/PCBM/TiO<sub>2</sub>/FTO structure by using a metal mask from the glove box, which was sent to the thermal evaporation equipment. The vacuum environment was  $4.8 \times 10^{-6}$  Torr, and the evaporation rate was 2.5–3.0 nm/s. Finally, a 100 nm thick Ag electrode was deposited on top of the spiro-OMeTAD/MAPbI<sub>3</sub>/PCBM/TiO<sub>2</sub>/FTO structure. The PSC device was constructed by using a MAPbI<sub>3</sub> active layer film through the two-step film-forming technology and thermal evaporation technology.

### 2.6. Performance Measurement

The field-emission scanning electron microscope (FE-SEM) images of the top and side of MAPbI<sub>3</sub>/TiO<sub>2</sub>/FTO and spiro-OMeTAD/MAPbI<sub>3</sub>/PCBM/TiO<sub>2</sub>/FTO structures at annealing temperatures of 80, 100, 120, and 140 °C were observed using FE-SEM (ZEISS Sigma, ZEISS, Munich, Germany), as illustrated in Figures 2 and 3, respectively. The X-ray diffraction (XRD) spectra of the MAPbI<sub>3</sub>/TiO<sub>2</sub>/FTO and spiro-OMeTAD/MAPbI<sub>3</sub>/PCBM/TiO<sub>2</sub>/FTO structures at annealing temperatures of 80, 100, 120, and 140 °C were measured using an X-ray diffractometer (X'Pert PRO MRD, PANalytical, Almelo, the Netherlands) for a  $2\theta$  from 10 to 60 as illustrated in Figure 4. The absorbance and transmittance spectra of MAPbI<sub>3</sub> at annealing temperatures of 80, 100, 120, and 140 °C were measured using a UV-VIS/NIR spectrophotometer (UH-4150, Hitachi, Tokyo, Japan) with a wavelength ranging from 400 to 1000 nm as illustrated in Figure 5. The photoluminescence (PL) spectra of MAPbI<sub>3</sub> at annealing temperatures of 80, 100, 120, and 140 °C were measured using a fluorescence spectrophotometer (F-7000, Hitachi, Tokyo, Japan) with a wavelength ranging from 400 to 1000 nm as illustrated in Figure 6. The current density–voltage (J–V) curves, PCE, fill factor (FF), short-circuit current ( $J_{sc}$ ), open-circuit voltage ( $V_{oc}$ ), and external quantum efficiency (EQE) performances of PSCs at annealing temperatures of 80, 100, 120, and 140 °C are displayed in Figure 7. The J–V curves of the devices were recorded using a Keithley 2420 source meter and a solar simulator (MFS-PV-Basic, Hong-Ming Technology Co., Ltd., New Taipei, Taiwan) producing 1 sun AM 1.5 (100 mW/cm<sup>2</sup>) sunlight. EQE was measured utilizing a spectral response measurement system (LSQE-R, LiveStrong Optoelectronics Co., Ltd., Kaohsiung, Taiwan).

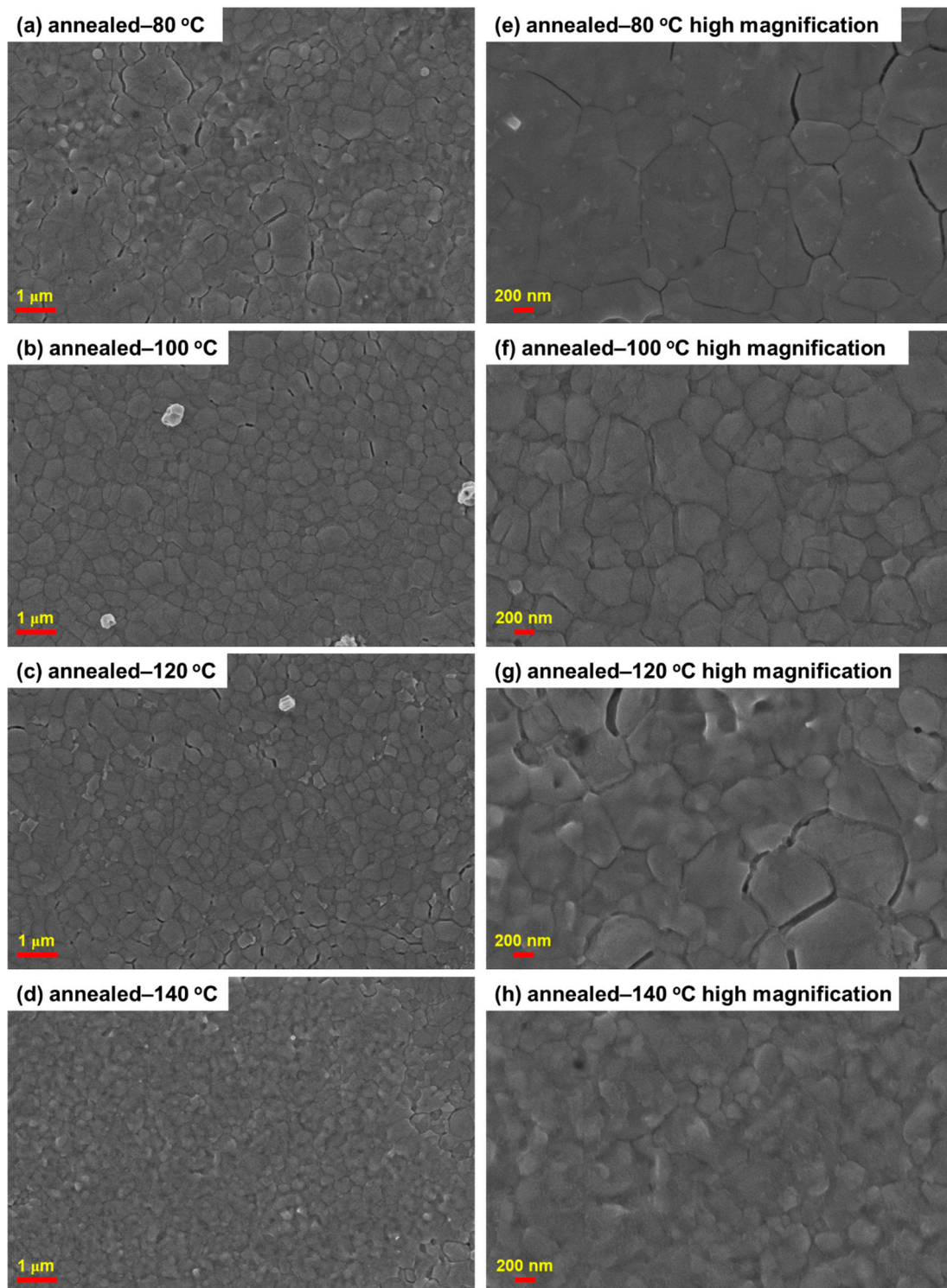


**Figure 2.** FE-SEM images of the top view of the MAPbI<sub>3</sub>/TiO<sub>2</sub>/FTO structure at different annealing temperatures, (a,e), (b,f), (c,g), (d,h), low and high magnifications annealed at 80, 100, 120, and 140 °C.

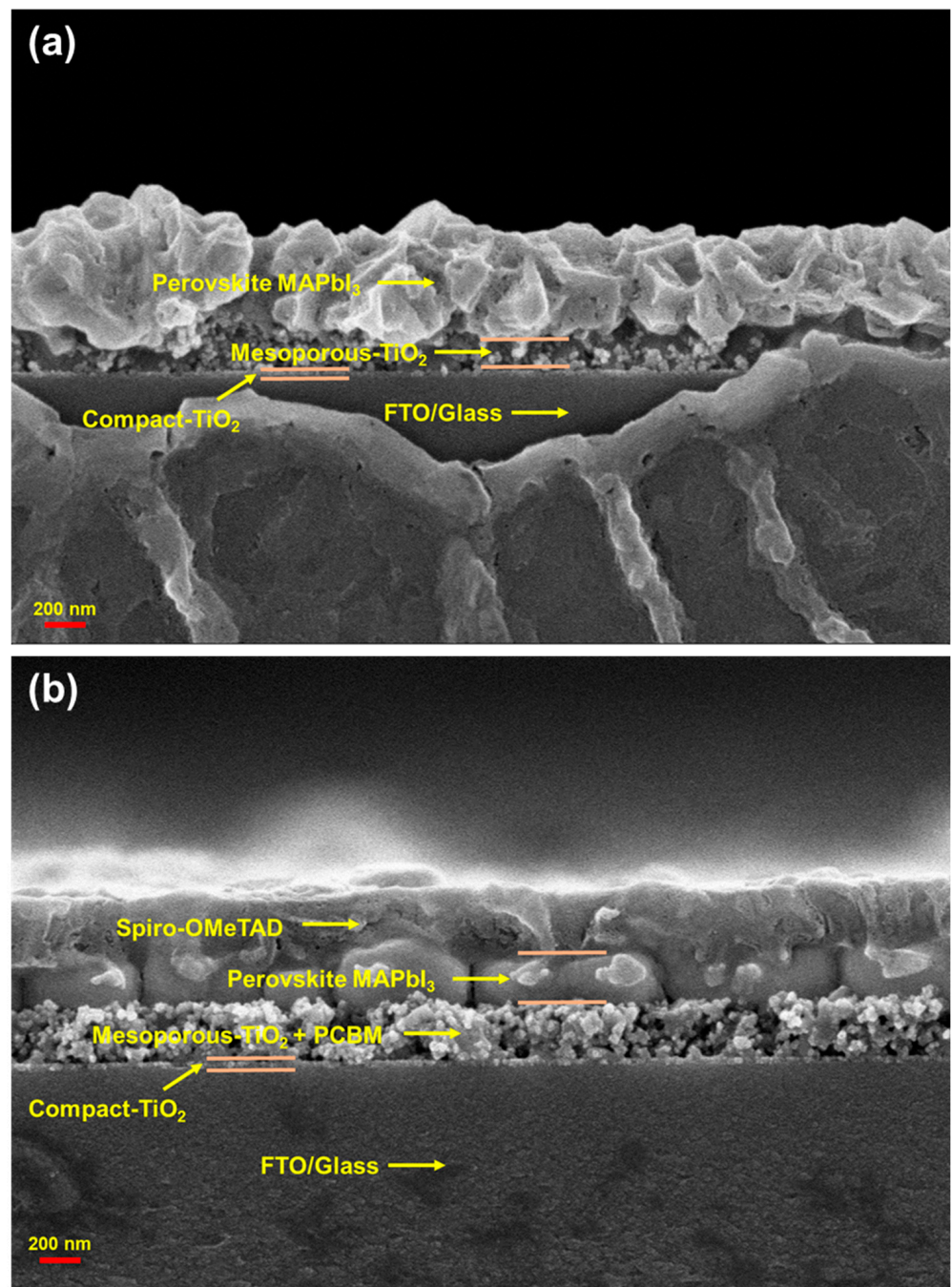


**Figure 3.** Cross-section FE-SEM images of (a) the MAPbI<sub>3</sub>/TiO<sub>2</sub>/FTO structure and (b) the spiro-OMeTAD/MAPbI<sub>3</sub>/PCBM/TiO<sub>2</sub>/FTO structure. The annealing temperature was 100 °C for 10 min.

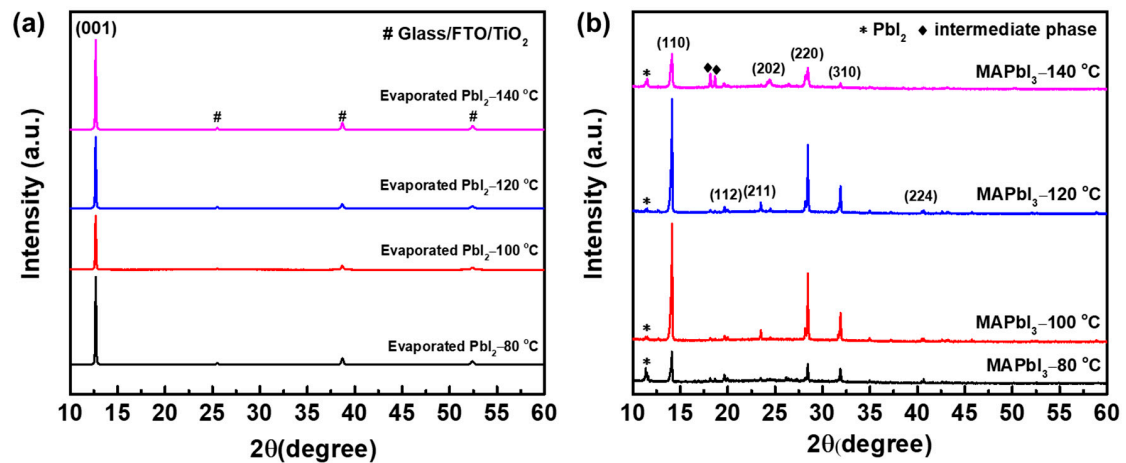


**Figure 4.** (a) The XRD spectrum of the  $\text{PbI}_2/\text{TiO}_2/\text{FTO}$  structure at treatment temperatures of 80, 100, 120, and 140 °C. (b) The XRD spectrum of the  $\text{MAPbI}_3/\text{TiO}_2/\text{FTO}$  structure at treatment temperatures of 80, 100, 120, and 140 °C.

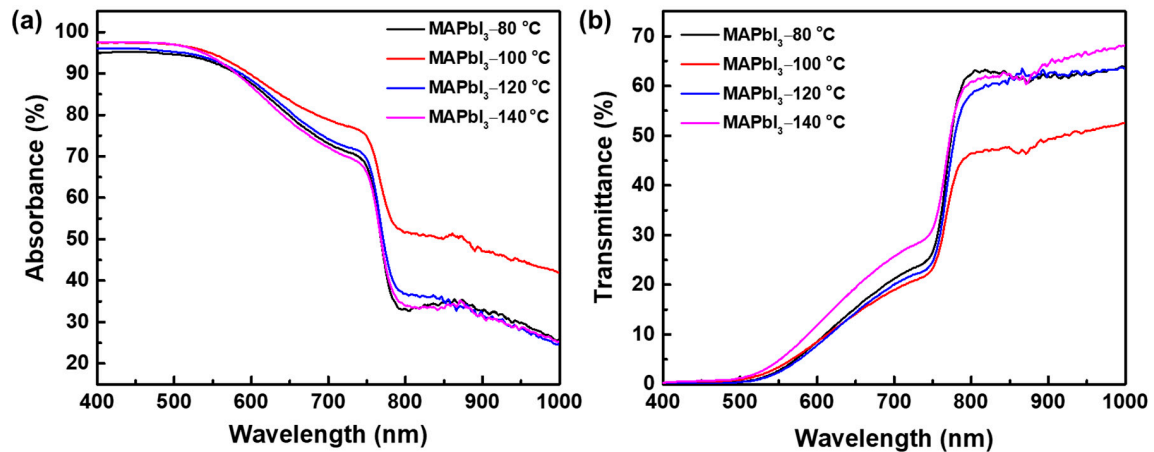


**Figure 5.** (a) Absorbance and (b) transmittance spectra of  $\text{MAPbI}_3$  at annealing temperatures of 80, 100, 120, and 140 °C.

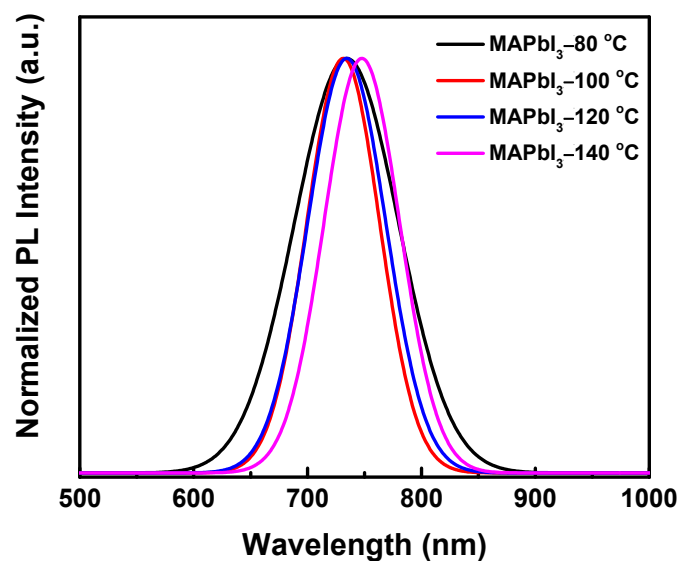


**Figure 6.** Photoluminescence (PL) spectra of the  $\text{MAPbI}_3/\text{TiO}_2/\text{FTO}$  structure at annealing temperatures of 80, 100, 120, and 140 °C.

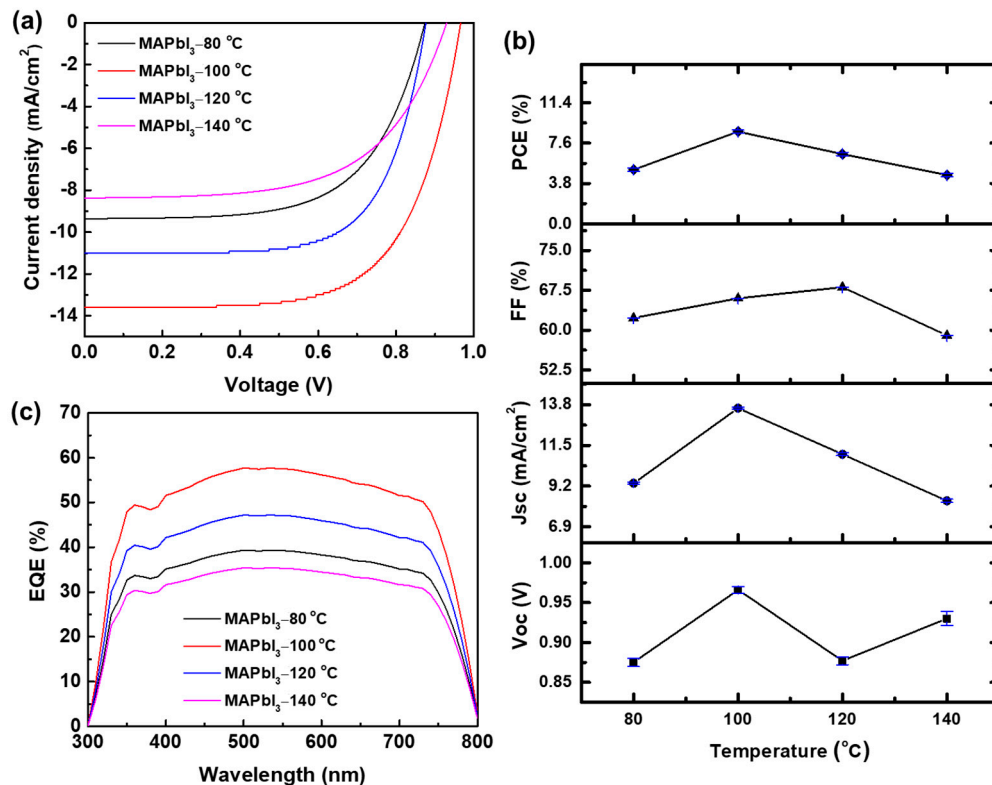


**Figure 7.** Device performance. (a) The illuminated J–V curves of the PSCs at annealing temperatures of 80, 100, 120, and 140 °C under forward scan. (b) They represent the corresponding PCE, FF, J<sub>sc</sub>, and Voc versus the temperatures at 80, 100, 120, and 140 °C. (The error bars were calculated from 20 devices). (c) EQE spectra.

### 3. Results and Discussion

FE-SEM images of the MAPbI<sub>3</sub>/TiO<sub>2</sub>/FTO and spiro-OMeTAD/MAPbI<sub>3</sub>/PCBM/TiO<sub>2</sub>/FTO structures are examined in Figures 2 and 3. Figure 2a–h displays the surface morphologies of the MAPbI<sub>3</sub> film. The PbI<sub>2</sub> crystal grains on the TiO<sub>2</sub>/FTO structure at annealing temperatures of 80, 100, 120, and 140 °C could be observed to have obvious different grain sizes, and some of them would aggregate into large clusters. A uniform perovskite film could be observed as the temperature increased owing to the fact that PbI<sub>2</sub> crystal lattices were changed with different annealing temperatures, making it easier to form them. This phenomenon was attributed to the weak Ti–I–Pb bonds facilitating the interfacial accommodation of moving iodine ions [23,29–31]. For MAPbI<sub>3</sub> films annealed at 80 and 140 °C, the resulting grain sizes were slightly reduced, and the gaps between the perovskite grains were more obvious, and pinholes became discernible. Therefore, relatively bright contrast grains appeared at the GBs, which might be residues caused by incomplete reaction or decomposition at a high annealing temperature. In addition, with the MAPbI<sub>3</sub> film annealed at 100 °C, the obtained film exhibited uniform and dense packed grains, which had almost no pinholes. However, the gap between the grains of the MAPbI<sub>3</sub> film annealed at 120 °C was also more obvious than that of the MAPbI<sub>3</sub> film annealed at 100 °C. This was consistent with the corresponding XRD pattern as discussed later. Figure 3a,b displays SEM images of the cross section of the MAPbI<sub>3</sub>/TiO<sub>2</sub>/FTO and spiro-OMeTAD/MAPbI<sub>3</sub>/PCBM/TiO<sub>2</sub>/FTO structures. A 250 nm thick MAPbI<sub>3</sub> film could be observed and well formed owing to the obvious TiO<sub>2</sub> porous layer, and the PCBM spin-coated on the porous layer formed a flat surface as illustrated in Figure 3b. The PCBM ETL played an important role in the decay of the photoinduced conductivity in MAPbI<sub>3</sub>/PCBM, which was on the time scale of hundreds of picoseconds to several nanoseconds, due to electron injection into PCBM and electron-hole recombination at the interface occurring at similar rates [32].

The measured XRD spectrum of the  $\text{PbI}_2/\text{TiO}_2/\text{FTO}$  structure is illustrated in Figure 4a at annealing temperatures of 80, 100, 120, and 140 °C. It could be found that the intensity of the  $\text{PbI}_2$  (001) plan at 12.6° was with a temperature increase [29,33,34]. This was owing to obvious decreased grain sizes and weak Ti–I–Pb bonds facilitating interfacial accommodation of moving iodine ions [23,29–31]. Figure 4b presents the XRD spectrum of  $\text{MAPbI}_3$  films at different annealing temperatures of 80, 100, 120, and 140 °C. The  $\text{MAPbI}_3$  film exhibited a main peak at 14.38°, which was the characteristic of the (110) plane in the tetragonal crystal structure, with other peaks corresponding to the (112), (211), (202), (220), (310), and (224) planes in the plot [33,34]. This was owing to the fact that  $\text{PbI}_2$  has a tetragonal crystal plan with strong diffraction peaks, which shows that the thin film was completely converted to perovskite  $\text{MAPbI}_3$  [29,30]. However, we noticed the presence of  $\text{PbI}_2$  diffraction peaks in the sample annealed at 80 °C, indicating that the started precursors (MAI and  $\text{PbI}_2$ ) were not completely converted. In addition, the perovskite/ $\text{PbI}_2$  XRD intensity ratio between the (110) plane of perovskite and the (001) plane of  $\text{PbI}_2$  diffraction peaks could be discussed to confirm whether the conversion was complete. A maximum ratio (24.15) was obtained with an annealing temperature of 100 °C, and the (001) peak of  $\text{PbI}_2$  was obviously weaker, which indicates that the MAI conversion was relatively complete and the PCE of PSC was more stable. On the other hand, the sample treated at an annealing temperature of 120 °C had the second best XRD intensity ratio (23.04). The  $\text{MAPbI}_3$  annealed at 140 °C had a slight phase transition and residual of  $\text{PbI}_2$  in the perovskite film, and there were unidentified peaks at 18.2° and 18.7° and so forth (indicated by black diamonds in Figure 4b). This indicates that the unidentified peak did not match the pure  $\text{PbI}_2$  or MAI tetragonal phase, which has existed as a not-well-described intermediate phase. In addition, the intensity of the perovskite diffraction peak of  $\text{MAPbI}_3$  annealed at 140 °C was weakened, and the intensity peak of the (001) plane characteristic diffraction peak of  $\text{PbI}_2$  was significantly increased. These results were the result of the decomposition of perovskite materials at a high annealing temperature, resulting in incomplete conversion of  $\text{PbI}_2$  and MAI, which seriously affected the PCE of PSCs [35–38]. The average crystallite size of the (110) plane was derived from the Scherrer formula, and the average crystal sizes at annealing temperatures of 80, 100, 120, and 140 °C were 43.32, 48.74, 48.12, and 31.44 nm, respectively. A maximum size of 48.74 nm was achieved at an annealing temperature of 100 °C, indicating that the optimum annealing temperature was 100 °C.

Figure 5a,b shows the absorbance and transmittance spectra of the  $\text{MAPbI}_3$  perovskite film annealed at 80, 100, 120, and 140 °C. The PL spectra of the  $\text{MAPbI}_3/\text{TiO}_2/\text{FTO}$  structure at annealing temperatures of 80, 100, 120, and 140 °C were measured at a wavelength range of 400 to 1000 nm, as illustrated Figure 6. A broad absorption spectrum was obtained, which corresponds to the energy gap of the PL diagram, and found that the absorption intensity at an annealing temperature of 100 °C was strongest, which was consistent with the results of XRD and PL analyses in Figures 4 and 6. The perovskite film annealed at 100 °C exhibited a small full width at half maximum (FWHM) of about 75.1 nm at the PL peak, which indicates the superior crystallinity of  $\text{MAPbI}_3$ , and the absorption strength was relatively high at this peak. On the other hand, we noticed that the PL peak of the perovskite film annealed at 140 °C had a red shift, which may be related to the reaction of  $\text{PbI}_2$  and MAI. It could be known from XRD analysis that under high temperature annealing, the  $\text{MAPbI}_3$  film decomposes into MAI and  $\text{PbI}_2$  double phase [39].

Finally, the J–V characteristic curves of PSCs were measured by forward scan as illustrated in Figure 7a, and the performance characteristic of the PSCs is illustrated in Figure 7b. It can be concluded that the degradation of device performance depends on the overall degradation of  $V_{oc}$ ,  $J_{sc}$ , and FF. However, it can be noted that when the annealing temperature of the  $\text{MAPbI}_3$  perovskite film prepared with the evaporated  $\text{PbI}_2$  film was 100 °C, the PSC showed a significantly improved photovoltaic performance. It can be found that the  $J_{sc}$  of the device prepared by annealing  $\text{PbI}_2$  at 100 °C was higher than that of the device prepared at 140 °C. It might be that the purity of the perovskite film prepared by annealing  $\text{PbI}_2$  at 100 °C was better, so it had higher absorbance, leading to

higher photocurrent. The smooth form of the perovskite film formed by PCBM could form a smaller charge transfer resistance. This form of film can not only increase the contact area between the perovskite and spiro-OMeTAD but also improve the PCE of PSCs. It was demonstrated that for the best performance of the PSCs at an annealing temperature of 100 °C for 10 min, PCE was about 8.66%,  $V_{oc}$  was 0.965 V,  $J_{sc}$  was 13.6 mA/cm<sup>2</sup>, and FF was 0.66. The  $V_{oc}$  of the PSCs at an annealing temperature of 140 °C reduced to 0.926 V, which may be due to the residual unconverted PbI<sub>2</sub> in the perovskite film. The passivation of PbI<sub>2</sub> could reduce the charge separation in defects, and the PbI<sub>2</sub> phase was presented. The perovskite grain boundary acted on the perovskite film in the PSC, resulting in an increase in the rate of charge extraction. Figure 7c shows the EQE spectra of the PSCs with various annealing temperatures. The integrated photocurrent densities from the EQEs were 9.29, 13.62, 11.14, and 8.36 mA/cm<sup>2</sup>, which are consistent with the corresponding J–V measurements in Figure 7a.

#### 4. Conclusions

In conclusion, a PSC with an organic perovskite active layer by using spin-coating and thermal vacuum evaporation technology was discussed and optimized by four annealing temperatures. From the SEM surface morphology, it could be observed that the morphology and size of perovskite obviously depend on the annealing temperature. High temperature forms large perovskite grains with random orientation, and the surface film forms a square crystal sparsely and unevenly. As the temperature changes, it could be seen that the perovskite film prepared close to 100 °C was dense and flat. In the XRD analysis, it was known that the PbI<sub>2</sub> (001) plan at 12.6° would change with the temperature. Meanwhile, the perovskite (110) plan at 14.38° displayed a strong X-ray diffraction intensity and tetragonal crystal at an annealing temperature of 100 °C. Therefore, a perovskite film of good quality could be obtained by changing the temperature of PbI<sub>2</sub>. After optimization, with the PCE,  $J_{sc}$ ,  $V_{oc}$ , and FF of the champion PSC device annealed at 100 °C, the perovskite film achieved 8.66%, 13.6 mA/cm<sup>2</sup>, 0.965 V, and 0.66. This work demonstrates a potential application of spin-coated and thermal vacuum evaporated MAPbI<sub>3</sub> films in planar organic–inorganic hybrid perovskite solar cells.

**Author Contributions:** L.-C.C. and Y.-T.C. carried out the experiments, designed the study, and gave significant suggestions on the whole manuscript. C.-H.T. and K.-Y.L. conceived the original idea, performed the data analysis and interpretation, and wrote the manuscript. Y.-S.T. prepared the samples and performed all the measurements. All authors have read and agreed to the published version of the manuscript.

**Funding:** This research was funded by MOST Nos. 109-2218-E-027-003-MY2 and 109-2622-E-027-031 and JiMei University Research Project under Contract No. Z91956/4412.

**Data Availability Statement:** Not applicable.

**Acknowledgments:** This research was supported by the Ministry of Science and Technology (Taiwan) under Contract Nos. 109-2218-E-027-003-MY2 and 109-2622-E-027-031 and JiMei University Research Project under Contract No. Z91956/4412.

**Conflicts of Interest:** The authors declare no conflict of interest.

#### References

1. National Renewable Energy Laboratory. Best Research-Cell Efficiencies. Available online: <https://www.nrel.gov/pv/assets/pdfs/best-research-cell-efficiencies.20200104.pdf> (accessed on 4 January 2021).
2. Lim, S.-H.; Seok, H.-J.; Kwak, M.-J.; Choi, D.-H.; Kim, S.-K.; Kim, D.-H.; Kim, H.-K. Semi-transparent perovskite solar cells with bidirectional transparent electrodes. *Nano Energy* **2021**, *82*, 105703. [CrossRef]
3. Wei, Z.; Smith, B.; De Rossi, F.; Searle, J.R.; Worsley, D.A.; Watson, T.M. Efficient and semi-transparent perovskite solar cells using a room-temperature processed MoOx/ITO/Ag/ITO electrode. *J. Mater. Chem. C* **2019**, *7*, 10981–10987. [CrossRef]
4. Islam, M.B.; Yanagida, M.; Shirai, Y.; Nabetani, Y.; Miyano, K. Highly stable semi-transparent MAPbI<sub>3</sub> perovskite solar cells with operational output for 4000 h. *Sol. Energy Mater. Sol. Cells* **2019**, *195*, 323–329. [CrossRef]

5. Ahmad, T.; Wilk, B.; Radicchi, E.; Pineda, R.F.; Spinelli, P.; Herterich, J.; Castriotta, L.A.; Dasgupta, S.; Mosconi, E.; De Angelis, F.; et al. New fullerene derivative as an n-type material for highly efficient, flexible perovskite solar cells of a p-i-n configuration. *Adv. Funct. Mater.* **2020**, *30*, 2004357. [[CrossRef](#)]
6. Yang, H.; Kwon, H.-C.; Ma, S.; Kim, K.M.; Yun, S.-C.; Jang, G.; Park, J.; Lee, H.; Goh, S.; Moon, J. Energy level-graded al-doped ZnO protection layers for copper nanowire-based window electrodes for efficient flexible perovskite solar cells. *ACS Appl. Mater. Interfaces* **2020**, *12*, 13824–13835. [[CrossRef](#)] [[PubMed](#)]
7. Tavakoli, M.M.; Yadav, P.; Prochowicz, D.; Tavakoli, R. Efficient, hysteresis-free, and flexible inverted perovskite solar cells using all-vacuum processing. *Sol. RRL* **2021**, *5*. [[CrossRef](#)]
8. Yang, D.; Yang, R.; Priya, S.; Liu, S. Recent advances in flexible perovskite solar cells: Fabrication and applications. *Angew. Chem. Int. Ed.* **2019**, *58*, 4466–4483. [[CrossRef](#)] [[PubMed](#)]
9. Wang, Y.; Jia, C.; Fan, Z.; Lin, Z.; Lee, S.-J.; Atallah, T.L.; Caram, J.R.; Huang, Y.; Duan, X. Large-area synthesis and patterning of all-inorganic lead halide perovskite thin films and heterostructures. *Nano Lett.* **2021**, *21*, 1454–1460. [[CrossRef](#)]
10. Zhao, Y.; Deng, Q.; Guo, R.; Wu, Z.; Li, Y.; Duan, Y.; Shen, Y.; Zhang, W.; Shao, G. Sputtered Ga-doped SnOx electron transport layer for large-area all-inorganic perovskite solar cells. *ACS Appl. Mater. Interfaces* **2020**, *12*, 54904–54915. [[CrossRef](#)]
11. Lee, D.-K.; Jeong, D.-N.; Ahn, T.K.; Park, N.-G. Precursor engineering for a large-area perovskite solar cell with >19% efficiency. *ACS Energy Lett.* **2019**, *4*, 2393–2401. [[CrossRef](#)]
12. Lai, X.; Meng, F.; Zhang, Q.; Wang, K.; Li, G.; Wen, Y.; Ma, H.; Li, W.; Li, X.; Kyaw, A.K.K.; et al. A bifunctional saddle-shaped small molecule as a dopant-free hole transporting material and interfacial layer for efficient and stable perovskite solar cells. *Sol. RRL* **2019**, *3*, 5. [[CrossRef](#)]
13. Liu, S.; Li, S.; Wu, J.; Wang, Q.; Ming, Y.; Zhang, D.; Sheng, Y.; Hu, Y.; Rong, Y.; Mei, A.; et al. Amide additives induced a fermi level shift to improve the performance of hole-conductor-free, printable mesoscopic perovskite solar cells. *J. Phys. Chem. Lett.* **2019**, *10*, 6865–6872. [[CrossRef](#)] [[PubMed](#)]
14. Yoo, J.J.; Seo, G.; Chua, M.R.; Park, T.G.; Lu, Y.; Rotermund, F.; Kim, Y.-K.; Moon, C.S.; Jeon, N.J.; Correa-Baena, J.-P.; et al. Efficient perovskite solar cells via improved carrier management. *Nature* **2021**, *590*, 587–593. [[CrossRef](#)]
15. Bowman, A.R.; Lang, F.; Chiang, Y.-H.; Jiménez-Solano, A.; Frohna, K.; Eperon, G.E.; Ruggeri, E.; Abdi-Jalebi, M.; Anaya, M.; Lotsch, B.V.; et al. Relaxed current matching requirements in highly luminescent perovskite tandem solar cells and their fundamental efficiency limits. *ACS Energy Lett.* **2021**, *6*, 612–620. [[CrossRef](#)] [[PubMed](#)]
16. Al-Ashouri, A.; Köhnen, E.; Li, B.; Magomedov, A.; Hempel, H.; Caprioglio, P.; Márquez, J.A.; Vilches, A.B.M.; Kasparavicius, E.; Smith, J.A.; et al. Monolithic perovskite/silicon tandem solar cell with >29% efficiency by enhanced hole extraction. *Science* **2020**, *370*, 1300–1309. [[CrossRef](#)] [[PubMed](#)]
17. Schulze, P.S.C.; Bett, A.J.; Bivour, M.; Caprioglio, P.; Gerspacher, F.M.; Kabakli, Ö.Ş.; Richter, A.; Stolterfoht, M.; Zhang, Q.; Neher, D.; et al. 25.1% high-efficiency monolithic perovskite silicon tandem solar cell with a high bandgap perovskite absorber. *Sol. RRL* **2020**, *4*, 2000152. [[CrossRef](#)]
18. Chen, B.; Yu, Z.J.; Manzoor, S.; Wang, S.; Weigand, W.; Yu, Z.; Yang, G.; Ni, Z.; Dai, X.; Holman, Z.C.; et al. Blade-coated perovskites on textured silicon for 26%-efficient monolithic perovskite/silicon tandem solar cells. *Joule* **2020**, *4*, 850–864. [[CrossRef](#)]
19. Si, F.; Tang, F.; Xue, H.; Qi, R. Effects of defect states on the performance of perovskite solar cells. *J. Semicond.* **2016**, *37*, 072003. [[CrossRef](#)]
20. Cao, K.; Li, H.; Liu, S.; Cui, J.; Shen, Y.; Wang, M. MAPbI3–xBrx mixed halide perovskites for fully printable mesoscopic solar cells with enhanced efficiency and less hysteresis. *Nanoscale* **2016**, *8*, 8839–8846. [[CrossRef](#)]
21. Wang, F.; Yang, M.; Zhang, Y.; Du, J.; Yang, S.; Yang, L.; Fan, L.; Sui, Y.; Sun, Y.; Yang, J. Full-scale chemical and field-effect passivation: 21.52% efficiency of stable MAPbI3 solar cells via benzenamine modification. *Nano Res.* **2021**, 1–7. [[CrossRef](#)]
22. Jung, M.-C.; Qi, Y. Dopant interdiffusion effects in n-i-p structured spiro-OMeTAD hole transport layer of organometal halide perovskite solar cells. *Org. Electron.* **2016**, *31*, 71–76. [[CrossRef](#)]
23. Jena, A.K.; Ikegami, M.; Miyasaka, T. Severe morphological deformation of spiro-OMeTAD in (CH3NH3)PbI3 solar cells at high temperature. *ACS Energy Lett.* **2017**, *2*, 1760–1761. [[CrossRef](#)]
24. Li, J.; Wang, H.; Chin, X.Y.; Dewi, H.A.; Vergeer, K.; Goh, T.W.; Lim, J.W.M.; Lew, J.H.; Loh, K.P.; Soci, C.; et al. Highly efficient thermally co-evaporated perovskite solar cells and mini-modules. *Joule* **2020**, *4*, 1035–1053. [[CrossRef](#)]
25. Roß, M.; Gil-Escrig, L.; Al-Ashouri, A.; Tockhorn, P.; Jošt, M.; Rech, B.; Albrecht, S. Co-evaporated p-i-n perovskite solar cells beyond 20% efficiency: Impact of substrate temperature and hole-transport layer. *ACS Appl. Mater. Interfaces* **2020**, *12*, 39261–39272. [[CrossRef](#)] [[PubMed](#)]
26. Kottokkaran, R.; Gaonkar, H.A.; Abbas, H.A.; Noack, M.; Dalal, V. Performance and stability of co-evaporated vapor deposited perovskite solar cells. *J. Mater. Sci. Mater. Electron.* **2019**, *30*, 5487–5494. [[CrossRef](#)]
27. Yang, W.S.; Noh, J.H.; Jeon, N.J.; Kim, Y.C.; Ryu, S.; Seo, J.; Seok, S.I. High-performance photovoltaic perovskite layers fabricated through intramolecular exchange. *Science* **2015**, *348*, 1234–1237. [[CrossRef](#)] [[PubMed](#)]
28. Liang, G.-X.; Fan, P.; Gu, D.; Zheng, Z.-H.; Zhang, D.-P.; Luo, J.-T.; Zhang, X.-H.; Ma, H.-L. Enhanced crystallinity and performance of CH3NH3PbI3 thin film prepared by controlling hot CH3NH3I solution onto evaporated PbI2 nanocrystal. *IEEE J. Photovoltaics* **2016**, *6*, 1537–1541. [[CrossRef](#)]

29. Zhu, N.; Qi, X.; Zhang, Y.; Liu, G.; Wu, C.; Wang, D.; Guo, X.; Luo, W.; Li, X.; Hu, H.; et al. High efficiency (18.53%) of flexible perovskite solar cells via the insertion of potassium chloride between SnO<sub>2</sub> and CH<sub>3</sub>NH<sub>3</sub>PbI<sub>3</sub> layers. *ACS Appl. Energy Mater.* **2019**, *2*, 3676–3682. [[CrossRef](#)]
30. Carrillo, J.; Guerrero, A.; Rahimnejad, S.; Almora, O.; Zarazua, I.; Mas-Marza, E.; Bisquert, J.; Garcia-Belmonte, G. Ionic reactivity at contacts and aging of methylammonium lead triiodide perovskite solar cells. *Adv. Energy Mater.* **2016**, *6*, 1502246. [[CrossRef](#)]
31. Xia, J.; Luo, J.; Yang, H.; Wan, Z.; Malik, H.A.; Shi, Y.; Yao, X.; Jia, C. Interface induced in-situ vertical phase separation from MAPbI<sub>3</sub>:Spiro-OMeTAD precursors for perovskite solar cells. *Sol. Energy Mater. Sol. Cells* **2020**, *216*, 110689. [[CrossRef](#)]
32. Ponceca, C.S.; Hutter, E.M.; Piatkowski, P.; Cohen, B.; Pascher, T.; Douhal, A.; Yartsev, A.; Sundström, V.; Savenije, T.J. Mechanism of charge transfer and recombination dynamics in organo metal halide perovskites and organic electrodes, PCBM, and spiro-OMeTAD: Role of dark carriers. *J. Am. Chem. Soc.* **2015**, *137*, 16043–16048. [[CrossRef](#)] [[PubMed](#)]
33. Jiang, Y.; Tu, L.; Li, H.; Li, S.; Yang, S.-E.; Chen, Y. A feasible and effective post-treatment method for high-quality CH<sub>3</sub>NH<sub>3</sub>PbI<sub>3</sub> films and high-efficiency perovskite solar cells. *Crystals* **2018**, *8*, 44. [[CrossRef](#)]
34. Wu, S.; Zheng, Y.; Liu, Q.; Li, R.; Peng, T. Low cost and solution-processable zinc phthalocyanine as alternative hole transport material for perovskite solar cells. *RSC Adv.* **2016**, *6*, 107723–107731. [[CrossRef](#)]
35. Wang, Y.; Mahmoudi, T.; Yang, H.-Y.; Bhat, K.S.; Yoo, J.-Y.; Hahn, Y.-B. Fully-ambient-processed mesoscopic semitransparent perovskite solar cells by islands-structure-MAPbI<sub>3</sub>-xClx-NiO composite and Al<sub>2</sub>O<sub>3</sub>/NiO interface engineering. *Nano Energy* **2018**, *49*, 59–66. [[CrossRef](#)]
36. Li, Y.; Zhang, T.; Xu, F.; Wang, Y.; Li, G.; Yang, Y.; Zhao, Y. CH<sub>3</sub>NH<sub>3</sub>Cl assisted solvent engineering for highly crystallized and large grain size mixed-composition (FAPbI<sub>3</sub>)<sub>0.85</sub>(MAPbBr<sub>3</sub>)<sub>0.15</sub> perovskites. *Crystals* **2017**, *7*, 272. [[CrossRef](#)]
37. Shan, D.; Tong, G.; Cao, Y.; Tang, M.; Xu, J.; Yu, L.; Chen, K. The effect of decomposed PbI<sub>2</sub> on microscopic mechanisms of scattering in CH<sub>3</sub>NH<sub>3</sub>PbI<sub>3</sub> films. *Nanoscale Res. Lett.* **2019**, *14*, 208. [[CrossRef](#)]
38. Jiang, Y.; Pan, L.; Wei, D.; Li, W.; Li, S.; Yang, S.-E.; Shi, Z.; Guo, H.; Xia, T.; Zang, J.; et al. The modified multi-step thermal annealing process for highly efficient MAPbI<sub>3</sub>-based perovskite solar cells. *Sol. Energy* **2018**, *174*, 218–224. [[CrossRef](#)]
39. Chen, L.-C.; Lee, K.-L.; Wu, W.-T.; Hsu, C.-F.; Tseng, Z.-L.; Sun, X.H.; Kao, Y.-T. Effect of different CH<sub>3</sub>NH<sub>3</sub>PbI<sub>3</sub> morphologies on photovoltaic properties of perovskite solar cells. *Nanoscale Res. Lett.* **2018**, *13*, 140. [[CrossRef](#)]